Toward global mapping of river discharge using satellite images and at-many-stations hydraulic geometry

Colin J. Gleason[1] and Laurence C. Smith

Department of Geography, University of California, Los Angeles, CA 90095-1524

Edited by James S. Famiglietti, University of California, Irvine, CA, and accepted by the Editorial Board February 18, 2014 (received for review September 17, 2013)

Rivers provide critical water supply for many human societies and ecosystems, yet global knowledge of their flow rates is poor. We show that useful estimates of absolute river discharge (in cubic meters per second) may be derived solely from satellite images, with no ground-based or a priori information whatsoever. The approach works owing to discovery of a characteristic scaling law uniquely fundamental to natural rivers, here termed a river's at-many-stations hydraulic geometry. A first demonstration using Landsat Thematic Mapper images over three rivers in the United States, Canada, and China yields absolute discharges agreeing to within 20–30% of traditional in situ gauging station measurements and good tracking of flow changes over time. Within such accuracies, the door appears open for quantifying river resources globally with repeat imaging, both retroactively and henceforth into the future, with strong implications for water resource management, food security, ecosystem studies, flood forecasting, and geopolitics.

remote sensing | fluvial geomorphology | river hydrology | AMHG | river runoff

Some 80% of the world's population and 65% of its river ecosystems are threatened by insecure water supply, yet global knowledge of the river discharges upon which these depend is surprisingly poor (1, 2). For much of the world, river gauge measurements are rare, nonexistent, or proprietary. Even well-monitored countries have sparsely distributed networks, thus limiting current understanding of water losses along river courses, habitat changes, and flood risk (3, 4). Satellites, in contrast, provide spatially dense coverage globally, attracting calls for a global river discharge mapping capacity from space (5–10). However, previous efforts to estimate river discharge from remotely sensed observations have all required inclusion of some form of ancillary ground-based information, such as gauge measurements, bathymetric surveys, and/or calibrated hydrology models that are simply unavailable for most of the planet (11–18). To remove this dependence on ground-based information, we show that useful estimates of absolute river discharge (i.e., in units of cubic meters per second) may be derived solely from multiple satellite images of a river, with no ground-based or a priori information whatsoever, through use of a characteristic scaling law, here termed a river's at-many-stations hydraulic geometry (AMHG). As will be shown in this paper, AMHG effectively halves the number of parameters required by traditional hydraulic geometry, thus paving the way for remote estimation of a single remaining parameter—and thus river discharge—through repeated satellite image observations along a river course. The presence of AMHG is verified in 12 of 12 rivers examined, using 88 in situ gauging stations, three field-calibrated hydrodynamic models incorporating 772 field-surveyed bathymetric cross-sections, and 42 Landsat Thematic Mapper (TM) satellite images (*SI Text*, section S1, *Materials and Methods* and Tables S1 and S2). Following a description of width AMHG, an innovative satellite discharge estimation approach is demonstrated for three major rivers, the Athabasca (Canada), Mississippi (United States), and Yangtze (China), based solely on repeated Landsat TM satellite measurements of varying instantaneous river flow widths over geographic space and time.

A Rare Advance in Hydraulic Geometry Theory

The field of hydraulic geometry was first introduced by Luna B. Leopold and Thomas Maddock, Jr., over 60 y ago (19) and continues to engage researchers in water resources, geomorphology, fisheries, aquatic ecology, and related fields today. It describes functional power-law relationships that relate river flow width (w), mean depth (d), and mean velocity (v) to discharge (Q) in accordance with the now-classic three equations:

$$w = aQ^b, \quad [1]$$

$$d = cQ^f, \quad [2]$$

$$v = kQ^m, \quad [3]$$

where $a \cdot c \cdot k$ and $b + f + m$ are theoretically constrained to unity because $Q = wdv$. In practice, the coefficients a, c, and k, and exponents b, f, and m are derived empirically through repeated field measurements at a single river cross-section (called at-a-station hydraulic geometry or AHG), or for some fixed frequency of discharge between cross-sections either downstream or on other rivers (called downstream hydraulic geometry or DHG). The depth AHG (Eq. **2**) has enormous practical utility, with empirical determinations of c and f comprising the traditional calibrated rating-curve method used by the US Geological Survey (USGS) and other water-monitoring agencies for computing

Significance

Political and practical realities limit our knowledge of water resources in many parts of the world. Here, we present a radically different approach for quantitative remote sensing of river discharge (flow rate) that is enabled by advancing a classic theory of river hydraulics and adapting it for use with satellite or aerial images. Because no ground-based information is required, the approach holds promise for addressing pressing societal, ecological, and scientific problems through global mapping of river flow.

Author contributions: L.C.S. conceived the problem and revisit of at-a-station hydraulic geometry; C.J.G. discovered at-many-stations hydraulic geometry, devised the discharge estimation method, and performed analyses; and C.J.G. and L.C.S. shared equally in research design and authorship of the paper.

The authors declare no conflict of interest.

This article is a PNAS Direct Submission. J.S.F. is a guest editor invited by the Editorial Board.

Freely available online through the PNAS open access option.

[1]To whom correspondence should be addressed. E-mail: cjgleaso@ucla.edu.

This article contains supporting information online at www.pnas.org/lookup/suppl/doi:10.1073/pnas.1317606111/-/DCSupplemental.

discharge as a function of continuously recorded water depths. Throughout six decades of research, the *b*, *f*, and *m* exponents have received abundant study, particularly in the context of elucidating theoretical and physiographic controls on their values (e.g., refs. 20–22). Eventually, they were recognized as reflective of mainly the bathymetric shape of a river channel's cross-section and argued to be unpredictably variable and site-specific (23). The *a*, *c*, and *k* coefficients, however, remain widely regarded as artifacts of the best-fit process to generate AHG. Strikingly little attention has been paid to them despite attention called to this gap by prominent authors (23–25).

This paper advances scientific understanding of hydraulic geometry by identifying a previously unnoticed correlative relationship between a river's AHG *a*, *c*, and *k* coefficients and their corresponding *b*, *f*, and *m* exponents. The correlations are readily revealed by plotting *a*–*b*, *c*–*f*, and/or *k*–*m* AHG pairs for many spatially distributed locations along a river, for example, from thousands of in situ measurements of river flow width, depth, and velocity collected between January 1, 2004, and April 9, 2013, at 88 USGS gauging station cross-sections along six prominent rivers in the United States (Fig. 1). Because these correlations are obtained simply by aggregating local AHG parameter pairs from many distributed locations along a river, they are here termed "at-many-stations hydraulic geometry," or AMHG. Although somewhat reminiscent of DHG (in that it considers longitudinal trends), AMHG differs markedly from DHG because all discharge variations are considered (not a single, bankfull discharge), the correlations are log-linear (not log-log), and the trends reflected do not follow a downstream direction. Further support for this purely empirical observation is given through consideration of limits of Eqs. **1–3** (*SI Text*, section S2 and Fig. S1).

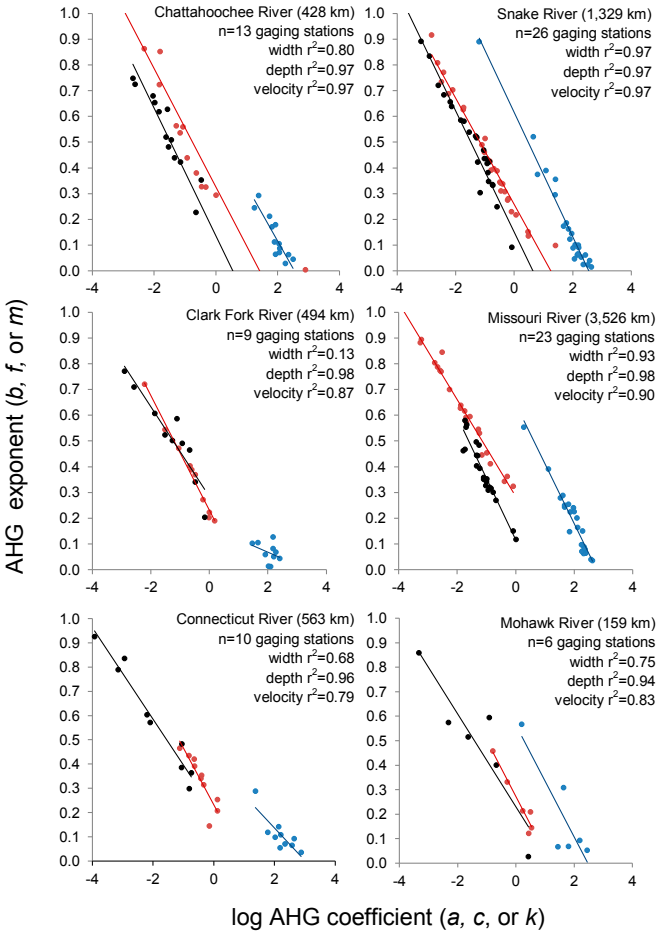

Fig. 1. AMHG derived from USGS field data. At-a-station hydraulic geometry (AHG) *a*, *c*, and *k* coefficients interact predictably with their corresponding *b*, *f*, and *m* exponents over long distances of a river, as revealed here from thousands of in situ measurements of flow width, depth, and velocity collected at 88 USGS gauging stations along six US rivers over the period 2004–2013. The discovery of these strong log-linear trends (blue, red, and black lines), here called at-many-stations hydraulic geometry or AMHG, effectively halves the traditional number of parameter(s) needed to compute river AHG and/or discharge, thus paving the way for satellite-based estimation of absolute river flow. Blue, width AMHG (*a* vs. *b*); red, depth AMHG (*c* vs. *f*); black, velocity AMHG (*k* vs. *m*).

Very significantly, the strong goodness-of fit for the observed AMHG relationships (i.e., r^2 = 0.94–0.98 for depth, r^2 = 0.13–0.97 for width, and r^2 = 0.79–0.97 for velocity; Fig. 1) indicates that, in contrast to prevailing thought (23), AHG coefficients and exponents are not unpredictable, but instead interact stably and predictably along long reaches of a river. This finding of robust depth, width, and velocity AMHG relationships essentially collapses the number of unknown AHG parameters in the three classical hydraulic geometry equations from six to three. If only one of a river's AMHG relationships is considered (as is commonly done in AHG, i.e., the traditional depth-discharge rating curve), then the number of unknown parameters is collapsed from two to one. For the purpose of river discharge estimation, this leads to the rather stunning conclusion that only one of the two traditional calibration parameters may suffice if a river's AMHG is well constrained. Although in principle any of a river's three AMHG relationships may be used for this purpose, we herewith focus on the *a*–*b* (width) AMHG, because unlike river depth or velocity, river width is straightforward to measure in satellite imagery.

Six other *a*–*b* relationships, plotted from output of field-calibrated Hydrologic Engineering Center–River Analysis System (HEC-RAS) hydrodynamic model simulations (Mississippi, Rio Grande, and Sacramento Rivers; *SI Text*, section S1) and/or simultaneous Landsat TM/gauging station observations (Mississippi, Athabasca, and Yangtze Rivers; *SI Text*, section S1) display similar behavior (r^2 = 0.60–0.99), further verifying the existence of this AMHG phenomenon (Fig. 2). Two of these datasets overlap a common area of the Mississippi River and yield virtually identical width-based AMHG, regardless of whether it is computed from a field-surveyed HEC-RAS hydrodynamic model or from Landsat TM images merged with gauging station measurements (Fig. 2, middle row, and Fig. S2). The derivation of a duplicate result from such different and independent datasets lends further support to the conclusion that AMHG scaling laws are a robust and valid characteristic of natural river behavior.

How Knowledge of a River's Width AMHG May Be Used to Estimate Discharge from Remotely Sensed Images

Based on this finding of a previously overlooked log-linear relationship between *a* and *b* (Figs. 1 and 2, and Fig. S2), the width AMHG for some user-defined length of river is appropriately defined as follows:

$$F = a_{x1,x2,\ldots xn} E^{b_{x1,x2,\ldots xn}}, \quad [4]$$

where the subscripts *x*1, *x*2,. . .*xn* correspond to spatially indexed cross-section locations (up to *n* total cross-sections along the river), *a* and *b* are the classic, site-specific AHG parameters at each cross-section, and *F* and *E* are river-specific constants defining the intercept and slope, respectively, of the empirical log-linear AMHG relationship calculated from all AHG *a*–*b* pairs. Knowledge of *E* gives the intercept as well as the slope of the AMHG relationship (as *F* may be approximated from measurement of cross-sectional widths along a river; *SI Text*, section S3

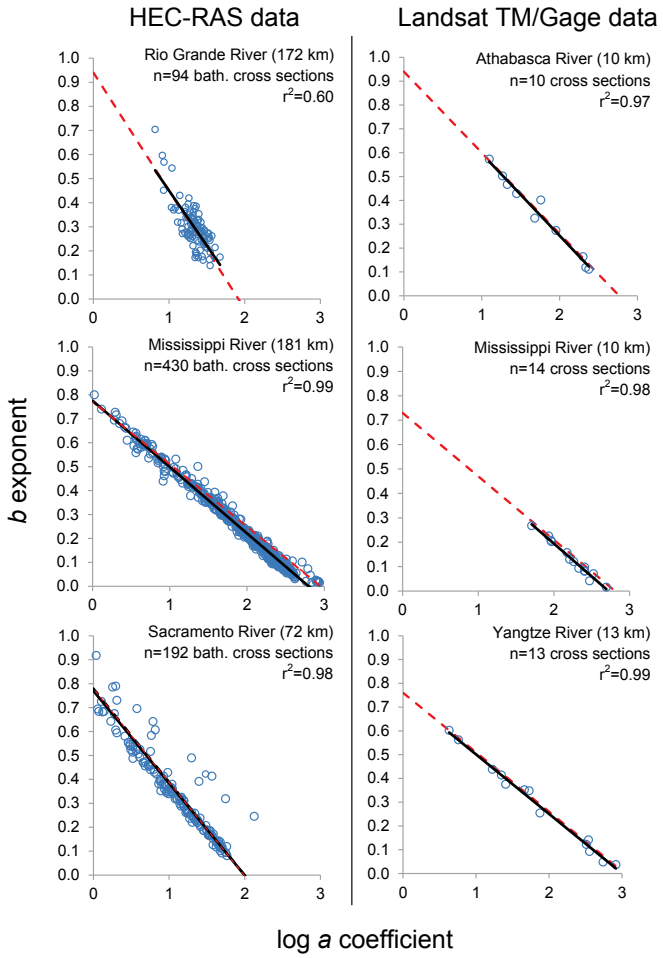

Fig. 2. AMHG derived from hydrodynamic modeling and from Landsat TM data. In situ width AMHG relationships (black lines) as derived from (*i*) simulations from three field-calibrated HEC-RAS hydrodynamic models for the Rio Grande, Mississippi, and Sacramento Rivers (United States) (left column); and (*ii*) instantaneous measurements of river surface width and discharge from Landsat Thematic Mapper (TM) satellite images over gauging stations at Fort McMurray, Alberta (Canada), Thebes, IL (United States), and Shashi, Hubei (China) (right column). The red dashed lines shows the width AMHG as approximated solely from measurements of surface width, with no knowledge of discharge or any other in situ information. The strong congruity between in situ and remotely estimated width AMHG forms the basis of quantitative remote sensing of river discharge from space.

and Table S3), thus allowing classical AHG *a* and *b* values everywhere along a sampled river length to be bridged using this single parameter *E*. Further mathematical discussion of AMHG and its relation to classic AHG parameters is provided in *SI Text* (section S3).

Critically, the width AMHG parameter *E* may be estimated from remotely sensed observations of river surface width accumulated over space and time (*SI Text*, sections S4 and S5 and Table S4), yielding remarkably accurate approximations of the river's width AMHG relationship compared with full in situ knowledge (red dashed lines, Fig. 2 and Fig. S2). From there, at least two approaches are available for computing absolute values (in cubic meters per second) of river discharge solely from satellite images: numerical optimization of AHG (as is recommended here; *SI Text*, section S7 and Fig. S3) or random seeding of plausible AHG values (*SI Text*, section S8 and Fig. S4). We here estimate local AHG from AMHG through heuristic optimization using a genetic algorithm (GA), a method that is both easily understood and parsimonious (26, 27). We adapted a previously developed GA (28) to minimize the difference in discharge calculated from AHG between pairs of cross-sections contained within ~10-km mass-conserved river reaches (i.e., without tributaries or outflows; *SI Text*, section S7), then reach-averaged these discharges to arrive at final reported hydrographs for six rivers (Fig. 3 and *SI Text*, section S9). Crucially, the methodology detailed in *SI Text*, section S7, requires only multitemporal measurements of cross-sectional width as input data, and draws AHG values from a wide range of possible values (Table S5) derived from each river's AMHG. The method assumes that AHG is valid for all cross-sections within each river reach, which is problematic when applied to rivers with large tidal or other backwater-controlled flow regimes. However, this purely remotely sensed approach differs markedly from previous discharge estimation methodologies in that no knowledge or assumptions about channel hydraulics (e.g., mean cross-sectional depth, roughness coefficient, or energy slope), local topography, or climatic conditions are needed to estimate river discharge.

Feasibility Demonstrations and Implications for Global Water Resources

The described satellite river discharge estimation procedure yields surprisingly good results, both in terms of absolute flow magnitude (in cubic meters per second) and its ability to track relative flow changes over time. For discharge estimates obtained solely from repeated Landsat TM measurements of instantaneous river surface width (Fig. 3), the mean reach-averaged discharge root-mean-square error (RMSE) is 2,585 m^3/s (23%), 299 m^3/s (30%), and 3,772 m^3/s (20%)

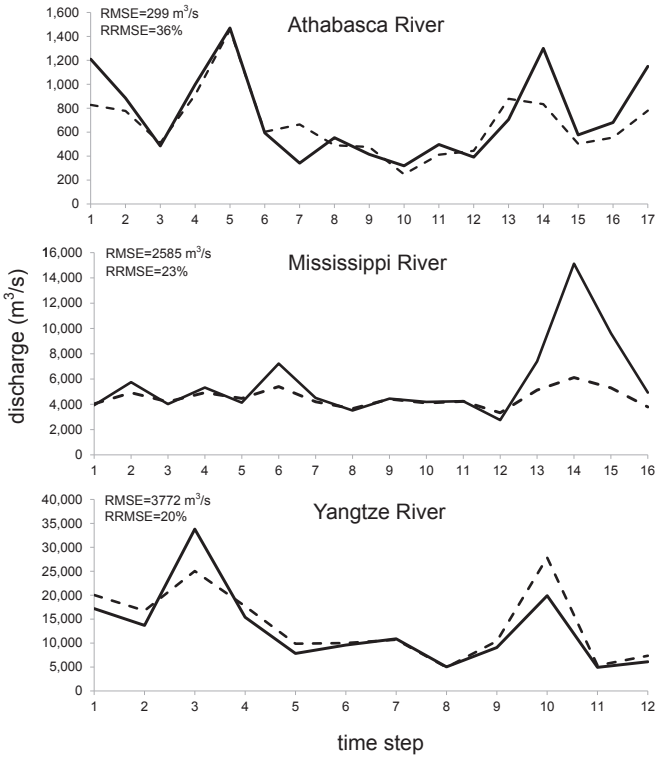

Fig. 3. Discharge estimation solely from Landsat TM images. Absolute (in cubic meters per second) river discharge hydrographs for 10- to 13-km reaches of the Athabasca, Mississippi, and Yangtze Rivers, as recorded by in situ gauging stations (solid line), and as estimated solely from Landsat TM satellite images (dashed line). The only data needed to produce the dashed-line hydrographs are repeated cross-sectional measurements of instantaneous river surface width collected over a river reach. Time step refers to chronological order of Landsat TM image acquisitions and thus varies for each river (for acquisition dates, see Table S2).

for a 10-, 10-, and 13-km reach of the Mississippi, Athabasca, and Yangtze Rivers, respectively, compared with independent discharge measurements collected at a permanent gauging stations contained within each reach (*SI Text*, section S9). These purely remotely sensed discharges also track temporal dynamics quite well (Fig. 3). The method does appear to underestimate discharges during large overbank floods (e.g., during a major June 10, 2008, event on the Mississippi River, time step 14 on Fig. 3), likely owing to breakdown of AHG power-law behavior when a river's flow overtops its banks (25).

For river discharge estimates obtained solely from repeated instantaneous surface widths output by the HEC-RAS hydrodynamic model, mean reach-averaged discharges yield similarly good results (Fig. S5), with RMSEs of 1,608 m^3/s (27%), 195 m^3/s (26%), and 29 m^3/s (1,083%) for the Mississippi, Sacramento, and Rio Grande Rivers, respectively (based on 15, 6, and 4 10-km reaches, respectively; Table S6). Like the Landsat TM results, these width-based discharge estimates also track temporal dynamics quite well (Fig. S5). Poorest performance is associated with the Rio Grande River, a semiarid, intermittently anabranching river with low flows, high geomorphic variability, and the second-weakest width AMHG seen in this study (r^2 = 0.60; Fig. 3). For further description of the sensitivities and performances of this discharge estimation method, see *SI Text*, section S9.

This paper presents an important and overlooked feature of a mature, widely used framework in water science, and uses it to advance a fundamentally different approach for estimating absolute river discharges (water fluxes) from space absent in situ measurements, calibrated hydrological models, or other a priori information. This directly mitigates a long-standing barrier of nonquantification of river flows for the vast majority of rivers on Earth, which impedes the efforts of scientists and policymakers to assess global vulnerabilities in human and ecosystem water security, compliance with transboundary river water-sharing agreements, water balance closure in climate models, flood probabilities, food chains, deforestation, and many other problems (1, 2, 29–32). Although the manually derived river width measurements described here are labor intensive, at least two methods exist for automated mapping of river widths from satellite imagery (33, 34). Merging of such automated width retrievals with the AMHG discharge estimation approach presented here would enable immediate commencement of approximate river discharge mapping for the world's large, single-thread rivers, using archived and/or forthcoming image data from aerial photographs, satellites, unmanned aerial vehicles, and any other source from which repeated images may be collected over large areas of the world's river systems.

ACKNOWLEDGMENTS. M. Durand and M. K. Mersel provided calibrated HEC-RAS model datasets, and J. Wang provided critical comments at an early stage of this research. M. Zebrowski provided graphical assistance with illustrations. Constructive, helpful reviews by two anonymous reviewers and N. D. Smith are gratefully acknowledged. This research was supported by National Aeronautics and Space Administration (NASA) Remote Sensing Theory Initiative Grant NNX12AB41G, with additional support from NASA Surface Water Ocean Topography Mission Grant NNX13AD88G, and NASA Earth and Space Sciences Fellowship NNX12AN32H.

1. Vörösmarty CJ, et al. (2010) Global threats to human water security and river biodiversity. *Nature* 467(7315):555–561.
2. Hannah DM, et al. (2011) Large-scale river flow archives: Importance, current status and future needs. *Hydrol Processes* 25:1191–1200.
3. Hunger M, Doell P (2008) Value of river discharge data for global-scale hydrological modeling. *Hydrol Earth Syst Sci* 12:841–861.
4. Stahl K, Tallaksen LM, Hannaford J, van Lanen HAJ (2012) Filling the white space on maps of European runoff trends: Estimates from a multi-model ensemble. *Hydrol Earth Syst Sci* 16:2035–2047.
5. Alsdorf DE, Lettenmaier DP (2003) Geophysics. Tracking fresh water from space. *Science* 301(5639):1491–1494.
6. Bjerklie DM, Dingman SL, Vorosmarty CJ, Bolster CH, Congalton RG (2003) Evaluating the potential for measuring river discharge from space. *J Hydrol (Amst)* 278:17–38.
7. Alsdorf DE, Rodriguez E, Lettenmaier DP (2007) Measuring surface water from space. *Rev Geophys* 45:RG2002.
8. Durand M, et al. (2010) The surface water and ocean topography mission: Observing terrestrial surface water and oceanic submesoscale eddies. *Proc IEEE* 98:766–779.
9. Syed TH, Famiglietti JS, Chambers DP (2009) GRACE-based estimates of terrestrial freshwater discharge from basin to continental scales. *J Hydrometeorol* 10:22–40.
10. Syed TH, Famiglietti JS, Chambers DP, Willis JK, Hilburn K (2010) Satellite-based global-ocean mass balance estimates of interannual variability and emerging trends in continental freshwater discharge. *Proc Natl Acad Sci USA* 107(42):17916–17921.
11. Smith LC, Isacks BL, Forster RR, Bloom AL, Preuss I (1995) Estimation of discharge from braided glacial rivers using ERS-1 SAR: First results. *Water Resour Res* 31:1325–1329.
12. Smith LC (1997) Satellite remote sensing of river inundation area, stage, and discharge: A review. *Hydrol Processes* 11:1427–1439.
13. Smith LC, Pavelsky TM (2008) Estimation of river discharge, propagation speed, and hydraulic geometry from space: Lena River, Siberia. *Water Resour Res* 44:W03427.
14. Bates PD, Horritt MS, Smith CN, Mason D (1997) Integrating remote sensing observations of flood hydrology and hydraulic modelling. *Hydrol Processes* 11:1777–1795.
15. Getirana ACV, et al. (2009) Hydrological monitoring of poorly gauged basins based on rainfall-runoff modeling and spatial altimetry. *J Hydrol (Amst)* 379:205–219.
16. Biancamaria S, et al. (2011) Assimilation of virtual wide swath altimetry to improve Arctic river modeling. *Remote Sens Environ* 115:373–381.
17. Durand M, Rodriguez E, Alsdorf DE, Trigg M (2010) Estimating river depth from remote sensing swath interferometry measurements of river height, slope, and width. *IEEE J-STARS* 3:20–31.
18. Brakenridge GR, et al. (2012) Calibration of satellite measurements of river discharge using a global hydrology model. *J Hydrol (Amst)* 475:123–136.
19. Leopold LB, Maddock T (1953) *The Hydraulic Geometry of Stream Channels and Some Physiographic Implications*, USGS Professional Paper (US Government Printing Office, Washington, DC), Vol 252.
20. Knighton AD (1975) Variations in at-a-station hydraulic geometry. *Am J Sci* 275: 186–218.
21. Park CC (1977) World-wide variation in hydraulic geometry exponents of stream channels—analysis and some observations. *J Hydrol (Amst)* 33:133–146.
22. Parker G, Wilcock PR, Paola C, Dietrich WE, Pitlik J (2007) Physical basis for quasi-universal relations describing bankfull hydraulic geometry of single-thread gravel bed rivers. *J Geophys Res* 112:F04005.
23. Phillips JD (1990) The instability of hydraulic geometry. *Water Resour Res* 26:739–744.
24. Ferguson RI (1986) Hydraulics and hydraulic geometry. *Prog Phys Geogr* 10:1–31.
25. Dingman SL (2007) Analytical derivation of at-a-station hydraulic-geometry relations. *J Hydrol (Amst)* 334:17–27.
26. Grefenstette JJ (1986) Optimization of control parameters for genetic algorithms. *IEEE Trans Syst Man Cybern* 16:122–128.
27. Deb K, Pratap A, Agarwal S, Meyarivan T (2002) A fast and elitist multiobjective genetic algorithm: NSGA-II. *IEEE Trans Evol Comput* 6:182–197.
28. Gleason CJ, Im J (2012) A fusion approach for tree crown delineation from lidar data. *Photogramm Eng Remote Sensing* 78:679–692.
29. Trenberth KE, Fasullo JT (2013) North American water and energy cycles. *Geophys Res Lett* 40:365–369.
30. Forsythe FN, Fowler HJ, Kilsby CG, Archer DR (2012) Opportunities from remote sensing for supporting water resources management in village/valley scale catchments in the upper Indus basin. *Water Resour Manage* 26:845–871.
31. Sabo JL, Finlay JC, Kennedy T, Post DM (2010) The role of discharge variation in scaling of drainage area and food chain length in rivers. *Science* 330(6006):965–967.
32. Davidson EA, et al. (2012) The Amazon basin in transition. *Nature* 481(7381):321–328.
33. Pavelsky TM, Smith LC (2008) RivWidth: A software tool for the calculation of river widths from remotely sensed imagery. *IEEE Geosci Remote Sens Lett* 5:70–73.
34. Fisher GB, Bookhagen B, Amos CB (2013) Channel planform geometry and slopes from freely available high-spatial resolution imagery and DEM fusion: Implications for channel width scalings, erosion proxies, and fluvial signatures in tectonically active landscapes. *Geomorphology* 194:46–56.

Supporting Information

Gleason and Smith 10.1073/pnas.1317606111

SI Text

S1. Materials and Methods

We used datasets of in situ hydraulic measurements collected by the US Geological Survey (USGS), rating-curve–derived discharges published by Environment Canada and Changjiang Wuhan Waterway Bureau (China), simulations from three well-calibrated Hydrologic Engineering Center–River Analysis System (HEC-RAS) hydrodynamic models, and 42 archived Landsat Thematic Mapper (TM) satellite images to develop understanding of at-many-stations hydraulic geometry (AMHG) and a river discharge estimation method.

River Gauging Station Data. Field-measured datasets were acquired from the USGS (http://waterdata.usgs.gov/nwis) for six major American rivers (the Chattahoochee, Clark Fork, Connecticut, Missouri, Mohawk, and Snake Rivers). For each of these rivers, historical in situ measurements of river surface width, mean cross-sectional depth, mean cross-sectional velocity, and computed discharge were recorded at various stations (ranging from 6 to 26 stations) along the river by the USGS. The total river lengths along which these USGS station data were compiled ranged from 160 to 3,500 km. River reach lengths were calculated using the National Atlas' *Streamer* tool (http://nationalatlas.gov/streamer/Streamer/streamer.html) by subtracting the "downstream" distances between the most upstream and most downstream station for each river. All available measurements beginning January 1, 2004, were used to construct the three classical at-a-station hydraulic geometry (AHG) relationships (1) for width, depth, and velocity at each station. Field observations before this date were not used, so as to minimize the impact of changing channel geometry on the derived AHG relationships. Note also that only field-measured discharges were used in this dataset, not estimates of discharge from depth-discharge rating curves. Once each station's width, depth, and velocity AHG relationships were built (from discharge and the appropriate hydrologic variable), each AHG coefficient and exponent pair (one for each station) became one data point in the AMHG plots seen in Fig. 1. AHG exponents falling outside the range 0–1 (a total of 7 points) were removed from Fig. 1 for clarity, as these exponents represent failure of AHG to adequately describe fluvial behavior at their respective cross-sections. Table S1 supplies USGS station IDs of the gauging stations used for this part of the study.

Gauging station measurements of river discharge were also acquired for the Athabasca River below Fort McMurray, Alberta, Canada (Environment Canada gauge 07DA001, downloaded from http://environment.alberta.ca/apps/osip/). These discharge data were combined with measurements of instantaneous flow width manually digitized from simultaneously acquired Landsat TM images to determine both AHG (blue circles, Fig. 2) and AMHG (blue line, Fig. 2) as will be described shortly. Similarly, river gauge data were acquired for the Yangtze River at Shashi gauging station, Hubei, China (www.cjhdj.com.cn). Unlike the USGS data described above used to develop and test AMHG, discharge for the Canadian and Chinese stations was calculated using stage-discharge rating curve calibrated by occasional discharge surveys at these stations, a well-accepted methodology for publishing discharge data. These rating-curve data were used as field-measured data were not available for these stations. These datasets are primarily used to validate discharge estimation, and AMHG was first discovered and validated from the USGS field-measured datasets.

HEC-RAS Hydrodynamic Model Simulations. To generate realistic simulated datasets of river surface width, mean depth, and mean velocity as function of discharge, three previously compiled datasets containing a total of 772 field-surveyed bathymetric cross-sections for large reaches of three major American rivers (Rio Grande River: study length, 172 km, 94 cross-sections; Mississippi River: study length, 181 km, 430 cross-sections; Sacramento River: study length, 63 km, 192 cross-sections) were used. A range of discharges was simulated through these field-surveyed cross-sections using the HEC-RAS hydrodynamic model (version 4.1.0, downloaded from www.hec.usace.army.mil/software/hec-ras/) to generate instantaneous river surface widths, cross-sectional mean depths, and cross-sectional mean velocities for 20, 17, and 21 arbitrary time steps for the Rio Grande, Upper Mississippi, and Sacramento Rivers [Rio Grande and Mississippi HEC-RAS model output published in ref. 2 and provided by M. K. Mersel (US Army Cold Regions Research and Engineering Laboratory, Hanover, NH); Sacramento HEC-RAS model output provided by M. Durand (The Ohio State University, Columbus, OH)]. These model outputs enabled calculation of all three AHG coefficients and exponents at each cross-section in accordance with Leopold and Maddock (1). As with the USGS in situ datasets (Fig. 1), plotting each cross-section's AHG coefficient–exponent pairs enables determination of AMHG, with strong log-linear correlations found for width, depth, and velocity. For clarity, only the width-based AMHG is presented in Fig. 2.

Landsat TM Data. Archived Landsat TM images were used to measure instantaneous river surface widths surrounding gauging stations on the Mississippi, Athabasca, and Yangtze Rivers with 30-m spatial resolution, thus providing real-world satellite case studies from which to demonstrate AMHG and remote sensing of discharge. A 10-km reach of the Upper Mississippi River was chosen for study that is spatially coincident with the HEC-RAS–modeled dataset and extends 5 km upstream and downstream of the gauge at Thebes, IL. Sixteen Landsat TM scenes that were temporally coincident (same day) with in situ field-measured discharges at this USGS gauge (i.e., not estimated from its stage-discharge rating curve) were identified over the period 1999–2012 and downloaded from http://earthexplorer.usgs.gov/ (Table S2). For each image, instantaneous river surface widths were measured from the near-infrared spectral band (band 4, 760–900 nm) in ArcGIS.10 by manually digitizing line segments orthogonal to thalweg flow direction at 14 cross-sections spaced evenly throughout the reach. Next, classical width AHG was calculated for every cross-section, using the same-day discharge measurement acquired at the gauge. This procedure was also carried out for a 10-km reach of the Athabasca River extending 10 km downstream of the Environment Canada gauge below Fort McMurray, Alberta, Canada, and a 13-km reach of the Yangtze River below Shashi gauging station near the Three Gorges Dam, Hubei, China. Widths were measured at 10 evenly spaced cross-sections from 17 Landsat scenes collected between 1990 and 2011 for the Athabasca dataset, whereas widths were measured at 13 evenly spaced cross-sections from 12 Landsat scenes dating from 2004 to 2011 for the Yangtze dataset (Table S2). AHG relationships were derived from these manually measured widths and rating-curve–derived discharge data from the appropriate gauging station.

S2. Theoretical Limits of the Classical AHG Equations

To gain intuitive understanding of what AMHG represents in geomorphic terms, a physical understanding of what each of the

axes in Figs. 1 and 2 represent is required. There is clear consensus that the AHG b exponent represents both cross-sectional channel shape [as proved by Ferguson (3)] and also the proportion of discharge that is accommodated through adjustments in width (by definition). However, understanding of the physical meaning of the a coefficient remains elusive. In a thorough analytical examination, Dingman (4) found that a is correlated with several channel parameters (bankfull width, bankfull depth, energy slope, and generalized conductance coefficient), but these correlations are valid only at a specific cross-section for which the depth, slope, and width are artificially manipulated. To understand the meaning of a between cross-sections, a different conception of a is required. Substitution of w/Q^b for a (via Eq. **1**), and further substituting wdv for Q (by definition) shows that a is equivalent to

$$\frac{w^{1-b}}{d^b v^b} \qquad \textbf{[S1]}$$

at any cross-section, confirming that a can be written as a mathematical function of b even without invoking AMHG. This definition of a enables understanding of AMHG in terms of geomorphologically understood quantities (w, d, v, and b) by investigating the behavior of a at the theoretical limits of b. It is readily observable that

$$\lim_{b\to 1}\frac{w^{1-b}}{d^b v^b}=\frac{1}{\mathrm{dv}}. \qquad \textbf{[S2]}$$

For any river, this quantity will be relatively small, especially if v and d are greater than 1. AMHG suggests that a increases as b decreases, so it is expected that, at $b = 0$, the other theoretical limit of b, a will be much larger than it is when $b = 1$. In this case:

$$\lim_{b\to 0}\frac{w^{1-b}}{d^b v^b}=w, \qquad \textbf{[S3]}$$

where w is a quantity that is certainly larger than $1/dv$. Placing these mathematical conclusions into a geomorphic context suggests that, at high b values, where changes in width accommodate a large proportion of changes in discharge, the width term in Eq. **S1** dominates and leads to increasingly smaller values of a as the numerator tends to 1. Conversely, at very small b values, discharge changes are accommodated more by depth and/or velocity adjustments with almost no changes in width, driving a values higher as $d^b v^b$ tends toward 1 in the denominator, despite the general tendency for w to decrease with decreasing b values. This behavior is seen in Fig. S1, where AMHG is presented in linear (rather than log-linear) space and shows clear w-dominant and clear dv-dominant portions of the river separated into the two "limbs" of the graph.

S3. Mathematical Discussion of the Width AMHG and Its Relation to Classical AHG Parameters

The *slope* and *intercept* of the log-linear width-based AMHG may be encapsulated in a single parameter E, which in turn can be related to site-specific river widths and b exponents (the parameter F is also required, but F may be approximated by observations; see below).

Mathematically, the log-linear relationship shown in Figs. 1 and 2 must comply with Eq. **S4** (which is the same as Eq. **4**):

$$F = a_{x1,x2,\ldots xn}E^{b_{x1,x2,\ldots xn}}, \qquad \textbf{[S4]}$$

where the subscript $x1, x2,\ldots xn$ refers to a spatially indexed cross-section location, a_x and b_x are the classical AHG parameters for that location, and F and E are river-specific constants. We propose that F may be approximated by w_x, where w_x is the spatially indexed river surface width: a quantity that remains relatively constant in log space, allowing for the log-linear behavior of AMHG. Substituting w_x for F and rewriting Eq. **S4** yields another formulation for width-based AMHG:

$$b_x = -\frac{1}{\log(E)} * \log(a_x) + \frac{1}{\log(E)} * \log(w_x). \qquad \textbf{[S5]}$$

Eq. **S5** has identical form to the empirically observed AMHG, where $-1/(\log(E))$ is the *slope* of AMHG, and $1/(\log(E))$*log (w_x) is the *intercept*. Note that E, a previously unknown parameter, is constant and unique to each river. Because it is spatially constant and has variable units (i.e., E is a single value for a river or a reach of river and its units change at a cross-section with changing b exponents), it does not correspond to any known hydrologic quantity.

Our two formulations of width AMHG (Eq. **4** and Eq. **S5**) may be verified analytically using observed width and discharge to calculate a_x, b_x, and w_x, and the best-fit lines in Fig. 2 to calculate the *slope* and *intercept* of each river's width-based AMHG.

Substituting *slope* for $-1/(\log(E))$ in Eq. **S5** gives

$$b_x = slope * \log(a_x) - slope * \log(w_x) \qquad \textbf{[S6]}$$

and

$$intercept = -slope * \log(w_x). \qquad \textbf{[S7]}$$

From Eq. **S7**, the logs of observed widths (w_x) multiplied by the observed best-fit *slope* must equate to the observed best fit *intercept* for each river to comply with both the behavior seen in Figs. 1 and 2 and the derivations of Eqs. **S4** and **S5**. Note that w_x is remarkably constant (in log space) for all rivers except the Rio Grande, which explains why it has the weakest a vs. b relationship of all rivers in Fig. 2. Strong congruity in peak values of histograms of *slope**log(w_x) and observed *intercept* values offer support that Eq. **S4** (AMHG formulation) is a valid summary representation of longitudinal hydraulic behavior as seen in Figs. 1 and 2 (Table S3).

S4. Estimation of the *E* Parameter from Remotely Sensed Images

Crucially, it is possible to estimate E solely from repeated measurements of instantaneous river surface width, collected simultaneously at multiple locations along a river. For all six datasets for which such simultaneous width data are available (i.e., Fig. 2; described in section S1), we observe that the difference of the squares of maximum and minimum observed widths at all cross-sections display power-law behavior with maximum observed widths, i.e.:

$$max\left(w_{x1,x2,\ldots,xn}\right) = p\left(max\left(w_{x1,x2,\ldots,xn}\right)^2 - min\left(w_{x1,x2,\ldots,xn}\right)^2\right)^y, \qquad \textbf{[S8]}$$

where p and y are derived empirically by fitting Eq. **S8** to the maximum/minimum width differences for all cross-sections in the same manner as F and E are obtained in Eq. **4**. Note that $max(w_x)$ appears on both sides of the equality in Eq. **S8** to yield an explicit formulation for y. Also note that the exponent y of this relationship has near-equivalence to E in Eq. **4** for all six simultaneously measured datasets (Table S4).

A mathematical proof for this congruity between E and y has not yet been found. However, we identify at least two factors that support use of y as an approximation of E. The first of these is a mathematical argument as follows:

Because the log-linear form of AMHG has a constant slope, it may be said that

$$slope = \frac{\Delta b}{\Delta \log(a)}. \qquad \textbf{[S9]}$$

Rewriting Eq. **S9** between any two points as

$$slope = \frac{b_{x2} - b_{x2}}{\log\left(\frac{a_{x2}}{a_{x1}}\right)}, \quad \textbf{[S10]}$$

where x_1 and x_2 refer to any pair of cross-sections along river, and substituting $w_x/Q_x^{b_x}$ for a_x gives the following:

$$slope = \frac{b_{x2} - b_{x1}}{\log\left(\frac{w_{x2}}{Q_{x2}^{b_{x2}}} \Big/ \frac{w_{x1}}{Q_{x1}^{b_{x1}}}\right)}. \quad \textbf{[S11]}$$

We assume mass is conserved within ~10-km reaches with no tributaries or outflows present; therefore, $Q_{x1} = Q_{x2}$. Substituting Q for each of these quantities and simplifying the denominator of Eq. **S11** gives the following:

$$slope = \frac{b_{x2} - b_{x1}}{\log\left(\frac{w_{x2}}{w_{x1}}\right) - (b_{x1} - b_{x2})\log\left(\frac{Q}{Q}\right)}. \quad \textbf{[S12]}$$

Recognizing that $\log(Q/Q) = 0$, Eq. **S12** may be written as follows:

$$slope = \frac{b_{x2} - b_{x1}}{\log\left(\frac{w_{x2}}{w_{x1}}\right)}. \quad \textbf{[S13]}$$

Eq. **S13** suggests another geomorphic consequence of an observed AMHG, i.e., that the ratio of the difference in b values to the log ratio of widths at any two cross-sections along a river is constant, or nearly so. This helps explain why the y exponent in Eq. **5** offers such remarkable congruity with observed slope values. Remembering that p and y are empirical parameters determined by width variations at all cross-sections, rewriting Eq. **S8** in log space yields the following:

$$y = \frac{\log w_{xmax}}{\log\left(w_{xmax}^2 - w_{xmin}^2\right)} + \log p. \quad \textbf{[S14]}$$

Noting that p is constant, Eqs. **S14** and **S13** can be seen as inverse analogs, where a change in width sensitivity ($(b_{x2} - b_{x1})$ and $\log(w_{max}^2 - w_{min}^2)$) between cross-sections exists in a constant ratio with a measure of width ($\log(w_{x2}/w_{x1})$ and $\log(w_{max})$). These ratios act in opposite directions, as corresponding terms appear in the numerator of one equation and the denominator of the other, driving the change in sign between observed AMHG slopes and the width-based proxy y.

A second supporting factor for use of this proxy is its empirical stability. For each of the three HEC-RAS datasets (>90 field-surveyed cross-sections each), the exponent y does not change when random subsamples of cross-sections are used to generate the power law in Eq. **S8**, reflecting a robust relationship between observed widths. E is therefore readily approximated from space, because repeated, simultaneously acquired measurements of instantaneous river surface width at many locations along a river are easily obtained from multitemporal satellite imagery (thus giving maximum and minimum flow widths over some user defined period). How this proxy for E and subsequent knowledge of AMHG leads to discharge estimation from remotely sensed imagery is detailed in section S7.

The link between y and the slope of a river's AMHG area is an area for further research. It remains to be seen if this congruence will be replicated for rivers that exhibit extreme AHG behavior or for very small streams. In addition, it is difficult to understand Eq. **S8**'s theoretical relationship to AMHG when AMHG itself has not been derived.

S5. Demonstration of Reproducible Width AMHG from Three Different Datasets

The HEC-RAS and Landsat TM/USGS gauging station datasets for the Mississippi River (Fig. 2, *Middle*) cover an overlapping area, allowing for a direct comparison of width AMHG built from these two independent data sources. Also, by ignoring the USGS gauging station data, the remotely sensed proxy for AMHG (see previous section) may be independently compared with the HEC-RAS and Landsat TM/USGS in situ versions. These three datasets (Landsat-only AMHG approximation, USGS in situ, and HEC-RAS) yield nearly identical AMHG (Fig. S2), making a powerful argument that AMHG is indeed a robust phenomenon, as the discharge and width measurements in the HEC-RAS and Landsat TM/USGS datasets are completely independent and obtained through very different means. Furthermore, the Landsat TM-only AMHG (red dashed line, Fig. S2) shows close agreement with the two in situ datasets, lending further confidence that a river's width AMHG may be remotely approximated from space.

S6. AMHG in the Context of Published HG Literature

Reconstruction of AMHG from Previously Published AHG Data. Despite a rich tradition of AHG research (e.g., refs. 3 and 5–11), few studies publish coefficient values in addition to exponent values (as noted by both refs. 3 and 4), and fewer still publish a–b pairs longitudinally along a river. As such, it is difficult to use past published results to investigate AMHG. However, of those studies that do publish a–b pairs for multiple locations along a river, AMHG behavior is evident. For example, in data published for the Yellow River (12), we calculate width, depth, and velocity AMHG relationships that display r^2 values of 0.43, 0.82, and 0.69, respectively. These AMHG fits are not as strong as those presented in this study, which may be because the time period covered by ref. 12 is much longer (>30 y) than the datasets used in this study, and the authors highlight the high degree of morphological change (which deeply affects AHG parameters) in each cross-section of their study. However, AMHG is still evident in the published AHG data. Similarly, data from Reid et al. (13) exhibit width-based AMHG behavior in streams larger than 20 m in width (r^2 of 0.47, 0.43 for two different rivers). However, the streams in ref. 13 smaller than 20 m in mean width do not exhibit AMHG behavior; and published a–b data for two streams (<10 m wide) in Nanson et al. (14) similarly fail to display AMHG behavior.

The reason for this breakdown in AMHG for narrow streams may likely be traced to Eqs. **S2** and **S3** (section S2). Considering Eq. **S2**, a narrow stream may indeed have a product of depth and velocity less than 1 (m^2/s), in which case $1/dv$ becomes larger, not smaller, as b approaches 1. This is precisely the case in both datasets where AMHG is not observed (13, 14), as both the maximum observed depths and maximum observed velocities are indeed less than 1 (m or m/s). In addition, depth and velocity values that give a product less than 1 also predict a breakdown in Eq. **S3**, as width in these narrow rivers will not always be greater than $1/dv$.

Use of Empirical Flow Resistance Equations to Explain AHG and Implications for AMHG. Hydrologists have commonly investigated hydraulic geometry in the context of widely accepted empirical flow resistance equations like the Manning and Chezy equations (e.g., refs. 3, 4, 15, and 16). Such investigations usually assume some channel shape (e.g., rectangular, parabolic, triangular, or "natural"), control for other physical properties of the channel (e.g., depth, roughness, channel slope), and then apply empirical

flow resistance equations to define the relationships between width, depth, and velocity given the selected physical properties of the channel. By imposing a discharge on these manipulated cross-sections, hydrologists can ascertain the resulting effect on hydraulic geometry, either at-a-station or downstream. Such analyses reveal much about how a and b behave at-a-station, with Ferguson (3) and Dingman (4) providing excellent examples. However, although manipulating one cross-section in isolation illuminates the relationship between a and b at that station, this procedure cannot speak directly to this relationship between cross-sections—the key discovery embedded in AMHG. Furthermore, because AMHG trends do not occur in a downstream direction (i.e., the points on the AMHG lines in Figs. 1 and 2 do not plot according to their relative position along the river), any analysis that considers only the effects of upstream channel geometry on downstream response provides limited potential for analyzing AMHG. More research is needed to ascertain whether AMHG arises from a mathematical dependency between AHG power laws, or reveals something deeper about river behavior in general. In either case, the strong trends identified confirm that AMHG is a widely observable phenomenon in rivers larger than ~20 m wide and, from a practical standpoint, may be exploited for the purpose of discharge estimation.

S7. River Discharge Estimation from Coupling Width AMHG with Heuristic Optimization of Local AHG Parameters (Method 1)

Assumptions and Overview. The discharge estimation approach relies on using a remotely sensed estimate of a river's width AMHG to resolve local, site-specific AHG parameters (and hence discharge) at multiple cross-sections along a mass-conserved reach of river. The method requires two assumptions. The first is that classical site-specific power law AHG behavior is applicable to each individual cross-section along a river. Although Ferguson (3) proved that power-law AHG behavior is not required by first principles, he noted that empirical power-law behavior remains widely applicable for most natural rivers. Second, although we do not assume that discharge is conserved over the entire length of a river, we do assume it is conserved over short reaches (~10 km) with no tributaries or outflows, negligible evaporative losses, and negligible hyporheic exchange. This necessitates a definition of reach length where discharge may reasonably be assumed conserved under these assumptions, here arbitrarily defined as ~10 km if located between tributaries or outflows. We considered all unique (i.e., no cross-section appears in more than one reach) available reaches containing 10 cross-sections or more without tributaries or outflows for analysis. A total of 31 such reaches (4 on the Rio Grande, 17 on the Mississippi, 7 on the Sacramento, and 1 each for the Mississippi, Athabasca, and Yangtze Landsat TM datasets) were identified for discharge estimation.

Discharge estimates are generated by a genetic algorithm (GA) that optimizes values for a and b for each cross-section in a reach: this method only requires observed cross-sectional widths and remotely sensed AMHG to operate (sections S4 and S5). A global search space representing all possible a and b values, as defined by the ranges given in Table S5, is refined to include only those a and b values falling within a narrow envelope surrounding each river's remotely sensed AMHG. These smaller populations of a and b, which still contain a wide range of values for both parameters (note the ranges of a and b seen in Figs. 1 and 2), are passed to optimization via GA in conjunction with observed widths to minimize the difference in discharge between cross-sections. The GA arrives at one a–b pair per cross-section from this initial population, which gives discharge via Eq. **1**. These cross-sectional discharges are then averaged to arrive at a final, reach-averaged discharge. Detailed information describing each step of this process is described below.

How the Ranges for AHG Parameters Given in Table S5 Align with Previously Published Values. The AHG literature contains numerous published b values for rivers across a wide range of climatic and geomorphic settings (e.g., refs. 5 and 9). They range from very small [e.g., $b < 0.00$ (5)], to the very large [e.g., $b > 0.8$ (5)]. However, for most rivers, b values are found within the ranges in Table S5 (5, 9). As previously noted, far fewer a values have been published, and few studies even discuss a, so it is a more difficult parameter to ascribe ranges to in this study. As such, the ranges of a values ascribed in this study coincide with observed a values from all datasets, where $1 < a < 500$. The parameter ranges used in this study represent a broad range of possible outcomes that match published literature and do not result in artificial convergence for the method described below.

Step 1. For a pair of cross-sections within a reach, use a GA to converge upon a value for a and a value for b that best conserve discharge (as calculated from classical AHG and their observed multitemporal widths) between them. A GA is a numerical optimization method that mimics the processes of natural selection, mutation, and sexual reproduction through the interaction of basic units termed "genes" and "chromosomes." A chromosome contains of a set of genes, where each gene is a specific parameter needed to implement a procedure or solve a problem. In the GA implemented in this paper (17), each chromosome has four genes representing the classical AHG parameters for each cross-section in a pair of cross-sections selected for optimization (i.e., one a and one b for each of the two cross-sections). The GA begins with 10 such chromosomes, where each gene (AHG a or b) is randomly drawn from the solution space defined by a narrow envelope surrounding empirically derived width AMHG. Chromosomes are then combined with observed widths to confirm whether the randomly generated AHG yields reasonable discharge in conjunction with observed instantaneous river surface widths at each of the cross-sections. Chromosomes that generate discharges falling outside some (large) allowable range of discharge are discarded. Here, we assume an allowable range as follows:

$$\text{minimum allowable discharge} = [\text{minimum observed width} * 0.5\text{-m depth} * 0.1\ \text{m/s velocity}],$$

$$\text{maximum allowable discharge} = [\text{maximum observed width} * 10\text{-m depth} * 5\ \text{m/s velocity}].$$

This allowable discharge bound is reasonable for rivers of the size in this study, where observed widths range from 40 to ~1,500 m. For these rivers, the minimum and maximum depths and velocity imposed by these discharge constraints form what we feel are conservative maximum and minimum bounds on realistically feasible discharge (e.g., between 2 and 2,000 m^3/s for a 40-m-wide river, and between 75 and 75,000 m^3/s for a 1,500-m-wide river).

Any chromosome that is discarded for generating an unreasonably large or small discharge is replaced by a new chromosome randomly drawn from the solution space until all 10 chromosomes pass the discharge filter. Chromosomes are then ranked by their "fitness," here calculated as the percentage difference in discharge between the two cross-sections represented by the chromosome, in a process called "selection." Then, each of these chromosomes has a chance to undergo the processes of "crossover" and "mutation," based on GA parameterization (Table S5). In crossover, specific genes from certain chromosomes are exchanged, mimicking the mingling of DNA in sexual reproduction. In mutation, there is a small chance (the mutation rate, here set at 0.1, Table S5) that a random gene is randomly altered. The altered chromosomes are then reranked according to their fitness (discharge conservation) and the five least-fit chromosomes "die out" and are replaced with

another five chromosomes populated with random genes drawn from the AMHG solution space. Following this process of initial selection, crossover, mutation, and final selection and regeneration, the initial 10 chromosomes are said to have completed one generation. The GA is then run for 50 generations with parameters defined in Table S5 to yield four heuristically optimized AHG parameters, i.e., one *a*–*b* pair for each of the two cross-sections. For further description of this GA, see Gleason and Im (17).

Step 2. Repeat step 1 50 times to obtain 100 estimates of AHG for each cross-section in a pair. Each GA arrives at a mass difference-minimized (in percent difference of discharge between two cross-sections) AHG for both cross-sections in a pair (step 1). In principle, this minimized difference should occur when proposed AHG parameters at each of two cross-sections in a pair are identical to their true AHG parameters. Initializing 50 independent GAs for both cross-sections in the pair, each starting with random genes drawn from AMHG-defined solution space, results in 100 estimates of AHG for each cross-section.

Step 3. Permute steps 1–2 over geographic space, applying the GA to all possible pairwise combinations of cross-sections within a mass-conserved reach. This results in $(n^2 - n)$*100 GA selected estimates of AHG parameters for each cross-section, where n is the number of cross-sections within the 10-km reach.

Step 4. Aggregate the $(n^2 - n)$*100 AHG estimates to arrive at a final AHG for each of n cross-sections. The GA output must be distilled from the $(n^2 - n)$*100 ensemble AHG estimates provided by spatial permutation to a single AHG per cross-section. Although GA furnished AHG values approach true AHG values at each cross-section, small deviations in either AHG parameter from the true value will cause large errors in discharge retrieval due to the power-law behavior of AHG. To resolve this, we exploited the one-parameter nature of AMHG. Median *a* values furnished by the GA were used in conjunction with the remotely sensed AMHG approximation to calculate a corresponding *b* value for each cross-section. This process was repeated using median GA estimated *b* values and AMHG to calculate *a* values, giving two discharge estimates per reach. These discharge estimates are nearly identical to one another, confirming the one-parameter nature of AMHG.

Step 5. Compute discharge Q from the final selected AHG a and b. After AHG *a* and *b* were determined, the resultant parameters were applied to observed widths to estimate discharge at each cross-section, following Leopold and Maddock (1). This yielded n discharge estimates (one for each cross-section), the median of which was taken as reach-averaged discharge. This final reach-averaging step had the added benefit of further reducing error stemming from the sensitivity of cross-sectional power-law behavior.

Testing showed that 50 GAs represented a consistent performance plateau for all datasets, where additional GAs of more generations added much more processing time without improving the estimation result. The Athabasca and Sacramento datasets showed consistent performance from 1 GA to 50 GAs, whereas the other four datasets showed decreased error as more GAs were added until the 50 GA threshold. A graphic summary of the approach is given in Fig. S3.

The approach presented here relies on using observed cross-sectional widths in conjunction with AMHG to estimate discharge. Other remotely sensed observations could potentially be added as constraints during the genetic algorithm parameter search phase. For instance, including measurements of water surface slope [as will be provided by the forthcoming National Aeronautics and Space Administration/Centre National d'Etudes Spatiales Surface Water and Ocean Topography (SWOT) mission; see swot.jpl.nasa.gov] in conjunction with a wide range of plausible roughness values could form additional reasonable discharge limits that would constrain the range of possible output values from the GA. Similarly, observed stage (i.e., water surface elevations, which will also be provided by SWOT and can currently be obtained over very large rivers with ocean radar altimeters) could likewise be added to the estimation procedure to provide additional boundary conditions. Finally, the discharge conserved, pairwise permutation cross-sectional analysis technique proposed here could also be extended to other variables (i.e., depth) or discharge estimates based on measurement frameworks other than AHG. For example, previous work by Mersel et al. (2) also examines how internal correlations between river inundation width and mean cross-sectional flow depth might be used to remotely estimate depth, using both cross-sections and reach-averaging of natural rivers.

S8. River Discharge Estimation from Coupling Width AMHG with Randomly Seeded Local AHG Parameters (Method 2)

The explanatory power of AMHG also provides a framework for estimating discharge from random AHG parameters, as seen in Fig. S4. To produce the hydrographs in this figure, *a* values were calculated via AMHG from random (uniform distribution) *b* values (0.0–1.0) for each cross-section in all three Landsat TM datasets. Discharge was then calculated through each cross-section from this random *b* and paired *a* by applying observed widths and the classical AHG equation, as before. The median discharge across cross-sections was again taken to produce a final reach-averaged hydrograph, and 100 of these "random" hydrographs were generated to create the plots in Fig. S4 (red lines). These randomly seeded hydrographs show remarkable congruity to one another and track the dynamics of the true discharge quite well. This indicates that knowledge of AMHG alone could be sufficient to calculate discharge from observed widths with reasonable error. Of particular interest is the inability of any hydrograph to capture the same peaks in the gauge data that the GA method also failed to produce. However, the GA did produce hydrographs that are slightly more accurate [root-mean-square error (RMSE)] than the random suite of hydrographs, showing both the influence of the difference between the remotely sensed estimate of AMHG and true AMHG and the ability of GA optimization to provide more effective estimates of discharge than randomly seeded parameters.

S9. Discharge Estimation Performance

Performance of the described width-only discharge estimation approach was evaluated in several ways. First, the RMSE between the reach-averaged discharge estimates and field-calibrated HEC-RAS model discharges (Mississippi, Rio Grande, Sacramento Rivers) was computed. Second, the relative root-mean-square error (RRMSE) was computed, so as to place the absolute RMSE error (in cubic meters per second) in the context of each river's flow magnitude (in percentage). RRMSE is calculated in the same manner as RMSE, except that the error at each observation is defined as the relative error (raw residual divided by the true value). Finally, the sensitivity of the method to choices in cross-sections within a reach was evaluated for the Mississippi HEC-RAS dataset.

Discharge Estimation from HEC-RAS–Simulated Datasets of River Width. The method produced good estimates of discharge for those HEC-RAS datasets displaying a tight width-based AMHG (*a* vs. *b*) relationship ($r^2 = 0.96$ and 0.97 for the Sacramento, and Mississippi, respectively), with mean RRMSE less than 27% for both rivers (Table S6). For the Rio Grande River, which has a weaker ($r^2 = 0.60$) width AMHG relationship, the approach produced estimates of discharge with much larger relative errors (>500%). Although the extreme RRMSE values for the Rio Grande are inflated because of the very small discharge (<1 m^3/s) in the dataset, the absolute RMSE is 29 m^3/s. Fig. S5 and the RMSE values in Table S6 provide an additional description of the method's performance for the Rio Grande, giving more information than simply RRMSE values. For all three HEC-RAS

datasets, the method produces a hydrograph that tracks the dynamics of the "true" (i.e., simulated) hydrograph very well.

Discharge estimation was less accurate for the Rio Grande because the Rio Grande does not exhibit strong width AMHG behavior. Each discharge estimation uses AMHG to calculate the final *a* and *b* values at each cross-section (step 4), and this step produced additional error for the Rio Grande. This conclusion is supported by aggregating GA results differently: namely, using the GA estimated *a* and *b* values directly and ignoring AMHG. Direct GA AHG output produced discharge estimations with RMSE less than 10 m^3/s for all four reaches of the Rio Grande (9, 10, 8, and 7 m^3/s), representing a substantial improvement in estimation accuracy from the previous estimations (12–41 m^3/s) but is still a relatively poor estimation. Using the GA estimated *a* and *b* parameters directly for the other datasets resulted in discharge estimates with an increase in estimation error by a factor of 3–5, indicating that the controlling factor in discharge estimation error is the "tightness" of the observed width AMHG and the ability of the remotely sensed proxy to describe it.

Sensitivity of the Approach. The method is spatially robust for the HEC-RAS datasets, yielding similar RMSEs for 6, 15, and 4 reaches (~10 km each) spread out along 63, 172, and 181 km of the Sacramento, Mississippi, and Rio Grande Rivers, respectively. Note that the Sacramento and Mississippi HEC-RAS datasets each have one reach where discharge estimation was significantly poorer than in the other reaches. No metric has yet been found that predicts which reaches will produce accurate estimations of discharge, and sensitivity tests show that those reaches that produce poor estimates of discharge are as similarly insensitive to cross-sectional choice as are other reaches that perform well.

The sensitivity of the method to choices in cross-sections was tested for the upper Mississippi River, as this HEC-RAS dataset contains both the greatest number of 10-km reaches (17) and the greatest number of field-surveyed cross-sections within each reach (between 15 and 30). The discharge estimation RMSEs in Table S6 reflect use of all cross-sections (up to 30) within each reach, and several tests were run to investigate how these results might be affected by the selection of cross-sections for discharge estimation. First, we tested the sensitivity of the method to the number of input cross-sections by using 15 equally spaced cross-sections within each reach, and then tested method performance using 10 cross-sections along a variability gradient as defined by $w_{xmax}^2 - w_{xmin}^2$. These tests produced discharge errors consistent to reported errors in Table S6, indicating both the insensitivity of the method to a further reduction in cross-sections and the ability to estimate discharge from unequally spaced cross-sections. However, when the method was tested using the 10 most highly width-variable cross-sections, performance degraded substantially for several reaches (reaches 8, 9, and 10). These sensitivity tests reveal that, at least for the Mississippi HEC-RAS dataset, cross-section selection is not critical in achieving optimal performance and selecting cross-sections by their spacing or width variability does not materially improve performance.

S10. Concluding Remarks

Classical hydraulic geometry research suggests that the AHG coefficients and exponents of each cross-section are unrelated (1, 3, 16), yet the strong empirical relationships demonstrated in Figs. 1 and 2, and Fig. S2 clearly indicate otherwise. The demonstration of AMHG in 12 independent datasets, for rivers in different physiographic settings and spanning long length scales, suggests that AMHG is broadly descriptive of river behavior. In addition, all three classical AHG equations exhibit AMHG behavior, despite differences in how coefficients and exponents of these equations vary with river scale and cross-sectional geometry. This suggests that, although the classical AHG relationships do summarize local, site-specific channel conditions, they also exist within a larger, river-wide AMHG and are not fully independent of each other.

The in situ width AMHG derived from Landsat TM images/USGS gauge data of the upper Mississippi River is virtually identical to that derived from an overlapping, independent HEC-RAS dataset of the same areas (Fig. S2). Critically, the width AMHG approximated solely from Landsat TM is also virtually identical to the width AMHG built from both of these datasets (red dashed lines, Fig. 2, middle row, and Fig. S2). This high level of similarity between different datasets further suggests that the width AMHG captures fundamental information about channel scaling and geometric behavior in natural rivers. Further study is needed to determine why AMHG trends are preserved over such surprisingly long river lengths, if power-law approximations are also suitable for small and/or multithread rivers, if additional improvements in RMSE are possible through choices of reach length and selection, and if a depth AMHG (using *c–f* pairs) can aid discharge retrieval from satellites that measure water surface elevation [e.g., the forthcoming SWOT mission (18)]. A theoretical link between *y* and *E*, bridging the empirically robust metric and AMHG, also deserves more attention.

AMHG has been observed reach lengths varying from 10 km (in the Landsat datasets) to over 3,000 km (in the USGS datasets). The minimum reach length for which AMHG is observed has yet to be determined, but the HEC-RAS datasets verify that AMHG is relatively consistent between reaches, and that reach-based AMHG is also quite similar to river-wide AMHG. Future research on AMHG should investigate the scales at which it is expressed, as well as the fractal behavior of the phenomenon, i.e., if subreaches always exhibit AMHG consistent with river-wide AMHG.

The discharge estimation performance presented here is highly encouraging for future discharge-mapping applications. However, more research is needed to discern how the method performs for rivers exhibiting AHG behavior outside the ranges proposed in Table S5: those rivers where changes in width with respect to discharge are either miniscule (highly managed and channelized rivers) or gigantic (braided rivers flowing over noncohesive bed material) will require some updating of the methodology. In particular, in those rivers with extremely low width sensitivity, inverting the classical AHG equations will likely be difficult due to the exponential relationship between the *b* parameter, width, and discharge. Likewise, smaller rivers might exhibit discharge outside of the ranges imposed in section S7, but this will only occur in extreme situations, as with AHG parameters.

Despite these uncertainties, this research indicates that it is possible to estimate absolute river discharge to within demonstrated accuracies where no gauging stations, field-calibrated watershed models, or other more direct means of quantifying river flow exist. It is our hope that the discovery of AMHG and its associated discharge estimation method can aid understanding of fluvial science and water resources the world over.

1. Leopold LB, Maddock T (1953) *The Hydraulic Geometry of Stream Channels and Some Physiographic Implications,* USGS Professional Paper (US Government Printing Office, Washington, DC), Vol 252.
2. Mersel MK, Smith LC, Andreadis KM (2013) Estimation of river depth from remotely sensed hydraulic relationships. *Water Resour Res* 49:3165–3179.
3. Ferguson RI (1986) Hydraulics and hydraulic geometry. *Prog Phys Geogr* 10:1–31.
4. Dingman SL (2007) Analytical derivation of at-a-station hydraulic-geometry relations. *J Hydrol (Amst)* 334:17–27.
5. Park CC (1977) World-wide variation in hydraulic geometry exponents of stream channels—analysis and some observations. *J Hydrol (Amst)* 33:133–146.
6. Knighton AD (1974) Variation in width-discharge relation and some implications for hydraulic geometry. *Geol Soc Am Bull* 85:1069–1076.

7. Knighton AD (1975) Variations in at-a-station hydraulic geometry. *Am J Sci* 275:186–218.
8. Phillips PJ, Harlin JM (1984) Spatial dependency of hydraulic geometry exponenets in a subalpine stream. *J Hydrol (Amst)* 71:277–283.
9. Rhodes DD (1977) *b-f-m* diagram- graphical representation and interpretation of at-a-station hydraulic geometry. *Am J Sci* 277:73–96.
10. Rhodes DD (1978) World-wide variations in hydraulic geometry exponents of stream channels- analysis and some observations-comments. *J Hydrol (Amst)* 39:193–197.
11. Richards KS (1973) Hydraulic geometry and channel roughness—a nonlinear system. *Am J Sci* 273:877–896.
12. Ran LS, Wang SJ, Lu XX (2012) Hydraulic geometry change of a large river: A case study of the upper Yellow River. *Environ Earth Sci* 66:1247–1257.
13. Reid DE, Hickin EJ, Babakaiff SC (2010) Low-flow hydraulic geometry of small, steep mountain streams in southwest British Columbia. *Geomorphology* 122:39–55.
14. Nanson RA, Nanson GC, Huang HQ (2010) The hydraulic geometry of narrow and deep channels; evidence for flow optimization and controlled peatland growth. *Geomorphology* 117:143–154.
15. Parker G, Wilcock PR, Paola C, Dietrich WE, Pitlik J (2007) Physical basis for quasi-universal relations describing bankfull hydraulic geometry of single-thread gravel bed rivers. *J Geophys Res* 112:F04005.
16. Phillips JD (1990) The instability of hydraulic geometry. *Water Resour Res* 26:739–744.
17. Gleason CJ, Im J (2012) A fusion approach for tree crown delineation from lidar data. *Photogramm Eng Remote Sensing* 78:679–692.
18. Durand M, et al. (2010) The surface water and ocean topography mission: Observing terrestrial surface water and oceanic submesoscale eddies. *Proc IEEE* 98:766–779.

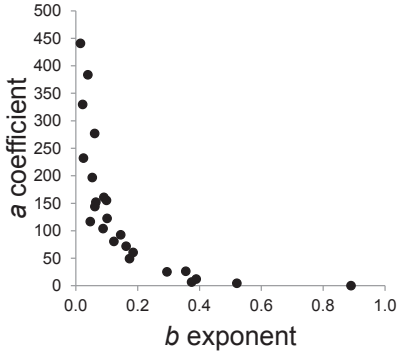

Fig. S1. AMHG behavior at its theoretical limits. Width-based AMHG for the Snake River reveals *w*-dominant ($b > 0.3$) and *dv*-dominant ($b < 0.2$) "limbs" in linear space, corresponding to the limits described in section S2.

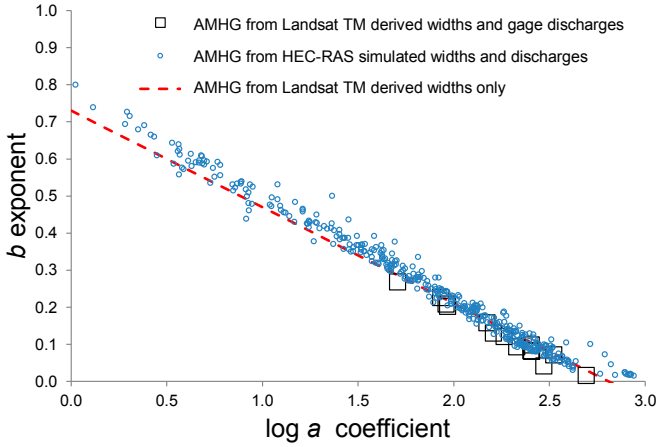

Fig. S2. Congruity between AMHG derived from three independent data sources. In situ width AMHG for the Upper Mississippi River near Thebes, IL, derived from two very different data sources shows remarkable congruity. The HEC-RAS width AMHG was built from imposing a range of simulated discharges through field-measured bathymetry to calculate instantaneous river width at multiple cross-sections. The Landsat TM/USGS AMHG was constructed from gauging station discharge and same-day Landsat TM-measured widths: there is no observed bathymetry. The Landsat TM-only AMHG was built following Eq. **5** and Eq. **S4** without gauge discharge. The only commonality between these datasets is the geometric form of the river's cross-sections (measured in HEC-RAS, implicit in Landsat TM), suggesting that AMHG, like AHG, is a geometric phenomenon that can furthermore be approximated solely from satellite observations.

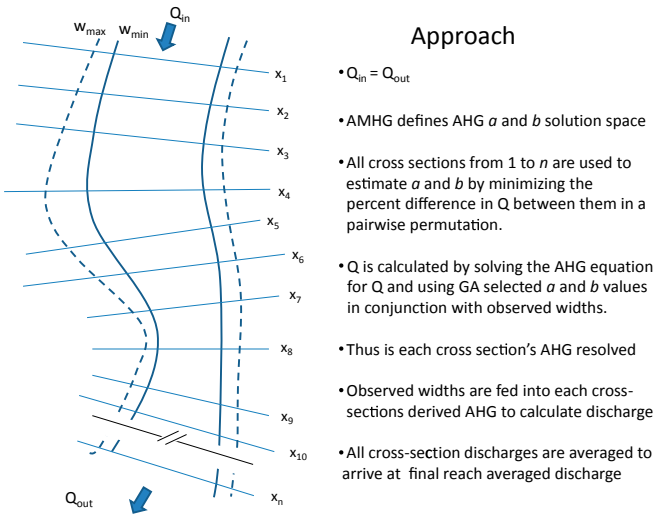

Fig. S3. Overview of the estimation approach. Schematic overview of the width AMHG discharge estimation method showing the basic principles of its operation, where *n* cross-sections in a mass-conserved reach are used to estimate AHG at each cross-section from candidate parameter variables derived from AMHG. Discharge is calculated at each cross-section by inverting its AHG with observed instantaneous flow widths, and then the median of these discharges is taken to arrive at a final, reach-averaged discharge.

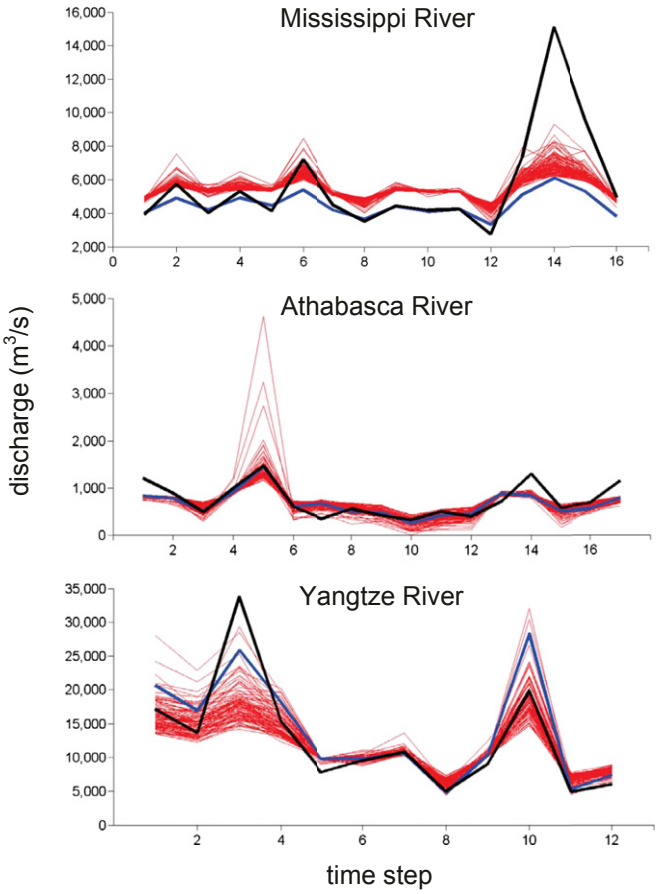

Fig. S4. Discharge estimation from randomly seeded AMHG. Reach-averaged river discharge hydrographs as estimated solely from river width information using a genetic algorithm (GA) (blue line) or 100 randomly seeded AHG pairs (red lines); and as recorded in situ by one gauging stations within the reach (black lines). The randomly seeded hydrographs were generated by imposing a random plausible *b* value (between 0.0 and 0.8) upon each cross-section and calculating the corresponding *a* value from AMHG, inverting this AHG pair to obtain cross-section discharge, and then taking the median of all cross-sections in the reach to arrive at a final reach-averaged discharge. The GA optimization procedure shows modest improvement over these randomly seeded hydrographs.

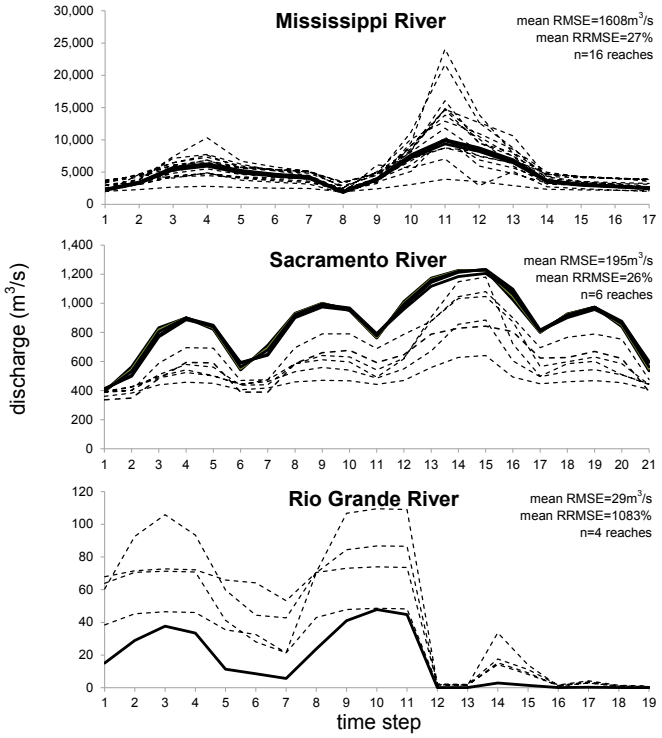

Fig. S5. Discharge estimation for three HEC-RAS–derived datasets. Hydrographs of estimated reach-averaged discharge (dashed lines) and known HEC-RAS–simulated discharge (solid lines) for the three HEC-RAS simulation datasets. Each dashed line represents a different, mass-conserved 10-km reach along the river corresponding to the rows in Table S6. Two outlier reaches with extreme errors are removed from the plot (reach 15 for the Mississippi and reach 4 for the Sacramento); Sacramento River reach 7 is also removed as its HEC-RAS–simulated discharge is noticeably anomalous from reaches upstream and downstream.

Table S1. Station IDs used to construct the AMHG in Fig. 1

River	Station ID	River	Station ID	River	Station ID
Chattahoochee (48)	02330450	Missouri (123)	06342500	Connecticut (60)	01184000
Chattahoochee (88)	02336000	Missouri (272)	06909000	Connecticut (54)	01138500
Chattahoochee (61)	02334430	Missouri (41)	06185500	Connecticut (44)	01144500
Chattahoochee (71)	02341505	Missouri (435)	06601200	Snake (27)	13334300
Chattahoochee (50)	02331600	Missouri (35)	06090800	Snake (67)	13022500
Chattahoochee (38)	02337170	Missouri (82)	06090300	Snake (101)	13062500
Chattahoochee (47)	02338500	Missouri (72)	06065500	Snake (85)	13081500
Chattahoochee (25)	02331000	Missouri (247)	06934500	Snake (67)	13154500
Chattahoochee (117)	02335815	Missouri (161)	06066500	Snake (20)	13135000
Chattahoochee (78)	02336490	Missouri (371)	06893000	Snake (45)	13087995
Chattahoochee (61)	02335000	Missouri (49)	06115200	Snake (87)	13077000
Chattahoochee (49)	02335450	Missouri (438)	06807000	Snake (31)	13171620
Chattahoochee (40)	02339500	Missouri (461)	06610000	Snake (20)	13153776
Chattahoochee (39)	02338000	Missouri (433)	06813500	Snake (61)	13094000
Mohawk (30)	01357500	Missouri (430)	06486000	Snake (75)	13057155
Mohawk (11)	01354500	Missouri (276)	06818000	Snake (71)	13018750
Mohawk (52)	01336000	Missouri (57)	06054500	Snake (86)	13037500
Mohawk (38)	01129440	Missouri (36)	06078200	Snake (74)	13032500
Mohawk (40)	01347000	Missouri (33)	06109500	Snake (73)	13010065
Mohawk (39)	01342602	Missouri (272)	06895500	Snake (21)	13090000
Clark Fork (68)	12353000	Missouri (43)	06177000	Snake (80)	13038500
Clark Fork (83)	12334550	Missouri (90)	06467500	Snake (75)	13057000
Clark Fork (39)	12391950	Connecticut (51)	01131500	Snake (77)	13013650
Clark Fork (86)	12324200	Connecticut (68)	01172010	Snake (61)	13011000
Clark Fork (39)	12331800	Connecticut (47)	01193050	Snake (91)	13069500
Clark Fork (94)	12323800	Connecticut (42)	01170500	Snake (29)	13172500
Clark Fork (92)	12324680	Connecticut (49)	01129500	Snake (69)	13213100
Clark Fork (48)	12389000	Connecticut (47)	01154500	Snake (74)	13060000
Clark Fork (60)	12354500	Connecticut (49)	01129200	Snake (26)	13290450
				Snake (36)	13269000

In situ measurements collected at these sites from January 1, 2004, to April 9, 2013, were used to derive classic AHG parameters and deduce the existence of AMHG. The number of measurements used in building AHG per gauging station is included in parentheses. A small number of AHG parameters (7 of 264) fell outside the expected range of 0–1, and these points were removed from Fig. 1.

Table S2. Image acquisition dates and scene IDs of Landsat TM images used in this study

Time step	Athabasca	Scene ID	Mississippi	Scene ID	Yangtze	Scene ID
1	5/28/1990	LT50430201990148PAC00	3/13/1996	LT50230341996073AAA01	10/9/2004	LE71240392004283EDC02
2	5/8/1991	LT50420201991128PAC00	8/20/1996	LT50230341996233XXX02	6/22/2005	LE71240392005173PFS00
3	10/6/1991	LT50430201991279PAC00	9/5/1996	LT50230341996249XXX00	8/25/2005	LE71240392005237PFS00
4	5/20/1993	LT50430201993140PAC01	8/7/1997	LT50230341997219AAA02	5/16/2006	LT51240392006136BKT00
5	5/15/1997	LT50430201997135PAC00	8/26/1998	LT50230341998238XXX01	8/20/2006	LT51240392006232IKR00
6	5/2/1998	LT50430201998122PAC00	7/20/1999	LE70230341999201PAC00	9/21/2006	LT51240392006264BKT01
7	10/18/1998	LT50420201998291PAC02	5/3/2000	LE70230342000124PAC02	10/21/2006*	LT51240392006296IKR00
8	5/31/2000	LE70430202000152EDC00	8/23/2000	LE70230342000236EDC00	3/23/2007*	LE71240392007083EDC00
9	10/6/2000	LE70430202000280EDC00	10/29/2001	LE70230342001302EDC00	5/18/2007*	LT51240392007139IKR00
10	10/31/2000	LE70420202000305EDC00	8/21/2002	LT50230341996233XXX02	8/15/2007	LE71240392007227EDC00
11	5/5/2002	LE70430202002125PAC00	10/16/2002	LE70230342002289EDC00	2/5/2008*	LE71240392008038EDC00
12	5/14/2002	LE70420202002134EDC00	9/9/2003	LT50230342003252PAC02	1/16/2009	LT51240392009016BJC00
13	5/21/2002	LE70430202002141EDC00	9/5/2005	LE70230342005249EDC00		
14	5/1/2003	LE70420202003121PAC00	6/10/2008	LE70230342008162EDC00		
15	10/10/2004	LE70420202004284EDC02	10/6/2010	LE70230342010279EDC00		
16	10/3/2010	LT50420202010276GLC02	6/5/2012	LE70230342012157EDC00		
17	5/15/2011	LT50420202011135PAC02				

*Same-day discharge data unavailable for these images. In situ data within ±2 d of image capture were used for these dates.

Table S3. A strong congruity between *slopelog(w_x) and the AMHG intercept is found for both HEC-RAS and Landsat TM datasets, suggesting that the parameter *F* in Eq. 4 is equivalent to (w_x) per Eq. S7**

Data source	River	Most frequent value of *slope**log(w_x)	Intercept of AMHG
HEC-RAS	Sacramento	0.78	0.77
	Mississippi	0.77	0.78
	Rio Grande	0.83	0.91
Landsat TM	Mississippi	0.77	0.74
	Athabasca	0.94	0.94
	Yangtze	0.76	0.75

Table S4. A strong congruity between the exponent *y* of Eq. S8 and slope of the width AMHG relationship is found for both HEC-RAS and Landsat TM datasets

Data source	River	*Slope* of log *a* vs. *b*	*y*	r^2 of Eq. **S8**
HEC-RAS	Sacramento	−0.39	0.39	0.97
	Mississippi	−0.28	0.26	0.80
	Rio Grande	−0.46	0.49	0.99
Landsat TM	Mississippi	−0.27	0.26	0.81
	Athabasca	−0.34	0.34	0.92
	Yangtze	−0.25	0.25	0.83

Table S5. Parameterization of the genetic algorithm used in this study

Parameter	Value
No. of generations	50
a min	1
a max	500
b min	0.01
b max	0.8*
Crossover rate	0.8
Mutation rate	0.1

*Maximum allowable *b* value derived from Park (1).

Table S6. Discharge estimation error per reach for HEC RAS generated datasets

	Mississippi HEC-RAS		Sacramento		Rio Grande	
Reach	RMSE, m^3/s	RRMSE, %	RMSE, m^3/s	RRMSE, %	RMSE, m^3/s	RRMSE, %
1	2,849	43.4	203	26.2	12	1,039.3
2	1,538	32.1	232	29.6	31	976.4
3	959	33.7	310	38.6	41	1,423.9
4	431	7.9	1,744*	202.8*	28	942.4
5	812	16.6	170	22.8		
6	411	6.7	84	12.3		
7	1,723	22.9	173	24.1		
8	1,851	38.8				
9	3,572	45.5				
10	1,172	18.1				
11	900	28.0				
12	1,580	35.1				
13	1,305	18.2				
14	1,282	14.3				
15	13,574*	154.8*				
16	3,740	39.7				
Mean	1,608	27	195	26	29	1,083

*Outlier reach removed in calculation of mean error statistic.